Journal of Materials Chemistry B

Comparison of the uptake of untargeted and targeted immunostimulatory nanoparticles by immune cells in the microenvironment of metastatic breast cancer

Journal:	*Journal of Materials Chemistry B*
Manuscript ID	TB-ART-10-2021-002256.R1
Article Type:	Paper
Date Submitted by the Author:	18-Nov-2021
Complete List of Authors:	Covarrubias, Gil; Case Western Reserve University School of Medicine, Biomedical Engineering Moon, Taylor; Case Western Reserve University, Biomedical Engineering Loutrianakis, Georgia ; Case Western Reserve University, Biomedical Engineering Sims, Haley; Case Western Reserve University, Biomedical Engineering Umapathy, Mayura ; Case Western Reserve University, Biomedical Engineering Lorkowski, Morgan; Case Western Reserve University School of Medicine, Biomedical Engineering Bielecki, Peter; Case Western Reserve University, Biomedical Engineering Wiesse, Michelle; Case Western Reserve University School of Medicine, Biomedical Engineering Atukorale, Prabhani; Case Western Reserve University School of Medicine, Biomedical Engineering Karathanasis, Efstathios; Case Western Reserve University School of Medicine, Biomedical Engineering

Comparison of the uptake of untargeted and targeted immunostimulatory nanoparticles by immune cells in the microenvironment of metastatic breast cancer

Gil Covarrubias[1,2†], Taylor J. Moon[1†], Georgia Loutrianakis[1‡], Haley M. Sims[1‡], Mayura P. Umapathy[1], Morgan E. Lorkowski[1], Peter A. Bielecki[1,2], Michelle L. Wiese[1], Prabhani U. Atukorale[1,2§], Efstathios Karathanasis[1,2*]

[1] Department of Biomedical Engineering, Case Western Reserve University, Cleveland, Ohio 44106, USA

[2] Case Comprehensive Cancer Center, Case Western Reserve University, Cleveland, Ohio 44106, USA

§ Current address: Department of Biomedical Engineering, University of Massachusetts, Amherst, MA 01003

† and ‡ Equal contribution

E-mail: stathis@case.edu

Abstract

To alter the immunosuppressive tumor microenvironment (TME), we developed an immunostimulatory nanoparticle (NP) to reprogram a tumor's dysfunctional and inhibitory antigen-presenting cells (APCs) into properly activated APCs that stimulate tumor-reactive cytotoxic T cells. Importantly, systemic delivery allowed NPs to efficiently utilize the entire microvasculature and gain access into the majority of the perivascular TME, which coincided with the APC-rich tumor areas leading to uptake of the NPs predominantly by APCs. In this work, a 60-nm NP was loaded with a STING agonist, which triggered a robust production of interferon β, resulting in activation of APCs. In addition to untargeted NPs, we employed 'mainstream' ligands targeting fibronectin, $\alpha_v\beta_3$ integrin and P-selectin that are commonly used to direct nanoparticles to tumors. Using the 4T1 mouse model, we assessed the microdistribution of the four NP variants in the tumor immune microenvironment in three different breast cancer landscapes, including primary tumor, early metastasis, and late metastasis. The different NP variants resulted in variable uptake by immune cell subsets depending on the organ and tumor stage. Among the NP variants, therapeutic studies indicated that the untargeted NPs and the integrin-targeting NPs exhibited a remarkable short- and long-term immune response and long-lasting antitumor effect.

Keywords: Immunostimulatory nanoparticles; STING agonist; interferon beta; metastatic breast cancer; immunotherapy

1 Introduction

Although metastasis occurs in about 30% of breast cancer (BC) cases, it disproportionally causes about 90% of BC-associated mortality. [1-4] Even worse, metastatic relapse is linked to the acquisition of pro-survival and chemoresistant phenotypes, thus making standard-of-care therapies ineffective against metastatic BC. Cancer immunotherapy is based on the premise of immune-recognition and targeted killing of tumor cells. In this context, immunotherapy also holds great promise to eliminate treatment-resistant metastases, [5] particularly in proinflammatory tumor microenvironments (TMEs) that contains functional antigen-presenting cells (APCs), such as dendritic cells (DCs) and macrophages. Unfortunately, a significant portion of cancer patients experience suboptimal responses to immunotherapies, stemming from their inability to overcome immunosuppressive signals that dominate the TME. [6-9] Importantly, BC cells can re-educate TME-associated innate and adaptive immune cells to acquire immunosuppressive phenotypes, resulting in the accumulation of dysfunctional and immunosuppressive APC, which generates a non-inflamed and unreceptive TME that shields the tumor from systemic immuno-surveillance.[10, 11] A potential strategy to overcome this immunosuppression relies upon robust stimulation of pro-inflammatory innate immunity within the TME, which can bridge the innate and adaptive arms of the immune system.[7-9]

Recent efforts have explored systemic delivery of immunostimulatory nanoparticles (NPs) that directly target, reprogram and activate the dysfunctional immune cells and local APCs in the TME, which can then facilitate an antitumor immune response leading to tumor clearance and prevention of disease relapse.[12-14] Systemic administration allows NPs to drain into the APC-rich perivascular niche of tumors, which leads to predominant uptake of NPs by the target subset of immune cells (Fig. 1A).[14] Further, systemic delivery is the most effective approach to access sites of metastasis. While nanoparticle-based delivery systems are typically focused on delivery of anticancer drugs to tumors, blood-circulating NPs are uniquely suited to reach APCs within the perivascular TME due to their ability to preferentially accumulate in these regions.

Here, we assessed the uptake of systemically administered immunostimulatory NPs by tumor-associated lymphocytes. The immunostimulatory NP consisted of a 60-nm nanoparticle loaded with cyclic diguanylate monophosphate (cdGMP),[15] an agonist of the stimulator of interferon genes (STING) pathway

(Fig. 1B). The STING agonist is a cyclic dinucleotide (CDN) that binds the STING machinery to trigger a robust production of Type I interferons leading to activation and expansion of APCs.[15-19] Specifically, we investigated the effect of different targeting ligands on directing immunostimulatory NPs to the perivascular TME and their respective uptake by different immune cell subsets in different breast cancer landscapes including early and late metastasis (Fig. 1C). Besides 'standard' non-targeted NPs, we developed NP variants using 'mainstream' targeting ligands that have been commonly used with nanoparticles in a conventional manner to deliver cancer drugs to tumor cells. As ligands, we selected three peptides targeting fibronectin, P-selectin or $\alpha_v\beta_3$ integrin. While these ligands have been widely employed for targeting nanoparticles to tumors,[20-25] they can also be suitable for directing NPs to immune cells in the near-perivascular TME. First, perivascular overexpression of fibronectin in the extracellular matrix plays a critical role in the migration of cancer cells.[26-29] Both non-targeted and fibronectin-targeting NPs preferentially deposit in the extracellular matrix of the TME and remain available for uptake by APCs. Next, P-selectin is an interesting target due to its overexpression by endothelial cells in the remodeled tumor vasculature.[30-35] STING activation of tumor endothelial cells has shown to generate strong antitumor response.[36, 37] Finally, while the role of integrins in angiogenesis, cancer progression and metastasis is well-known,[38] several integrins, including $\alpha_v\beta_3$, are expressed by dendritic cells and macrophages and mediate binding and phagocytosis.[39-41] We assessed the uptake of the four immunostimulatory NP variants by immune cells in three different breast cancer landscapes, including primary tumor, early metastasis and late metastasis. We used the 4T1 model, which is one of the standard models to study metastatic breast cancer in immunocompetent mice. We then characterized the cellular mechanisms of antitumor immune responses to the immunostimulatory NPs and the corresponding long-term therapeutic outcomes.

Fig. 1. *Illustration of targeting schemes for the delivery of immunostimulatory nanoparticles to tumors. (A) Systemic administration allows immunostimulatory nanoparticles to reach antigen-presenting cells in the near-perivascular area in sites of a primary tumor and metastasis. (B) Illustration of the 60-nm immunostimulatory nanoparticles loaded with a STING agonist (cdGMP). The distal ends of PEG coating can be used to link targeting ligands. (C) Schematic representation shows different immuno-stimulatory nanoparticle variants including untargeted, integrin-targeting, P-selectin-targeting and fibronectin-targeting. The microdistribution and uptake of the nanoparticle variants by different*

immune cell subsets is evaluated in three different breast cancer landscapes including primary tumor, early metastasis and late metastasis.

2 Chemicals and materials

2.1 Nanoparticle synthesis and characterization. Nanoparticles were developed by drying lipid films consisting of 48.5 mol% DOPC (1,2-dioleoyl-sn-glycero-3-phosphocholine, Avanti), 48.5 mol% DPPC (1,2-dipalmitoyl-sn-glycero-3-phosphocholine, Avanti), 3 mol% mPEG2000-DSPE (1,2-distearoyl-sn-glycero-3-phosphoethanolamine-N-[methoxy-(polyethylene glycol)-2000], Laysan Bio). Lipid films were hydrated using PBS at 60 ºC for 30 minutes and vortexed every 5-10 minutes. The nanoparticles were sized to 50-60 nm via ultra-sonication while under ice using a pulse sequence consisting of 10-second 20% power output intervals followed by a 20-second off cycle for a total of 5 minutes. Resultant nanoparticles were dialyzed for 2 h using a 50 kDA MWCO dialysis membrane against PBS and subsequently stored at 4 oC. Liposomal nanoparticles charge and size was ascertained using zeta potential and dynamic light scattering (DLS) measurements, respectively. The stock formulation was prepared at ~10^{15} particles/mL. Before these measurements, the samples were appropriately diluted to generate between 100-200 kcps. For fluorescently labelled nanoparticles a 0.5 mol% DiR (DiIC18(7) (1,1'-Dioctadecyl-3,3,3',3'-Tetramethylindotricarbocyanine Iodide)) dye was added during the lipid drying process by equally reducing the molar percentage of DOPC and DPPC. For treatment and immune cell recruitment studies, the dry lipid films were hydrated in 1X PBS containing 200 µg cyclic di-GMP (InvivoGen). Encapsulated cyclic di-GMP was measured via absorbance readings taken from a high-performance liquid chromatography (Shimadzu) assay. Drug retention studies were performed over a 24 h time course at 25 ºC.

Functionalization of nanoparticles with vascular targeting ligands was achieved through a sulfo-SMCC crosslinker. For these studies, the 3 mol% mPEG2000-DSPE was replaced with 3 mol% DSPE-PEG2000 Amine (1,2-distearoyl-sn-glycero-3-phosphoethanolamine-N-[amino(polyethylene glycol)-2000], Laysan Bio). As described previously, lipids films were developed, hydrated and ensuing nanoparticles were sized via ultra-sonication. Here the targeting ligands of interest were $\alpha v\beta 3$ integrins, P-selectins, and fibrin-based proteins using their targeting moieties; c(RGDfC), CDAEWVDVS, and CREKA,

respectively. Using sulfo-SMCC chemistry, we chemically linked the amine functionalized nanoparticles to the thiol groups of the previously indicated peptides. Available amine functional groups on the nanoparticle were linked to sulfo-SMCC and then the desired peptide in a 1:2:3 molar ratio, respectively, and allowed to react for 2.5 h. The molar ratio was consistent across all the peptide to secure similar peptide densities across the formulations. The nanoparticle-peptide constructs were dialyzed for 2 h using a 50 kDA MWCO dialysis membrane against PBS. To validate that the peptide density was similar, the number of peptides on each nanoparticle variant was measured using a Bio-Rad Protein Assay. Furthermore, particles were again subjected to DLS and zeta potential measurements to further guarantee consistency across nanoparticle batches. For treatment and immune cell recruitment studies, the resultant nanoparticle-peptide constructs were lyophilized until they were completely desiccated. The desiccated lipids were then re-hydrate in PBS containing 200 μg cyclic di-GMP (InvivoGen) followed by subsequent formulation steps. Cyclic di-GMP was incorporated after the nanoparticle-peptide conjugation and cleaning to prevent the exposed amine groups on cyclic di-GMP from participate in the functionalization reaction.

2.2 Animal care and use statement. All animal procedures were conducted under a protocol (#2015-0116) approved by the Institutional Animal Care and Use Committee of Case Western Reserve University. Animal well-being took priority over the studies conducted when it came to decisions regarding euthanasia or other interventions.

2.3 Tumor model. The 4T1 model was established in BALB/c mice (Jackson Laboratories). 4T1 cells were stably transfected with a lentivirus to express cytosolic firefly luciferase and green fluorescent protein (GFP). 4T1 cells were cultured in RPMI medium (Gibco, Gaithersburg, MD) containing 10% fetal bovine serum (FBS) and 1% penicillin-streptomycin. Cells were routinely tested for mycoplasma contamination to ensure cell line health and stability. Briefly, 4T1 inoculations were performed while mice were under a surgical anesthesia of 2-3% isoflurane inhalant. The no. 9 inguinal mammary fat pad was surgically exposed and an inoculant containing $5x10^5$ 4T1 cells/50 μL was injected. Tumors were closely monitored with bioluminescent imaging (BLI) and caliper measurements to track lesion progression. For tumor removals, mice were similarly anesthetized under a surgical plane. Solid tumors were surgically exposed and removed on either day 10 or 14 as described by the study. Meloxicam and bupivacaine were

administered pre- and post-surgery, respectively. Complete surgical resection was verified using bioluminescent imaging the day after tumor removal. In the case where mice were re-challenged, an inoculant containing $1x10^5$ 4T1 cells/50 µL was subcutaneously injected into the right flank. Tumor-bearing mice were intravenously treated with nanoparticles as indicated by the respective study. Cyclic di-GMP (InvivoGen) was administered at a 10 μg dosage. Anti-PD1 was subcutaneously administered adjacent to the solid tumor mass at a dosage of 250 µg (BioXCell).

2.4 Bioluminescent imaging. Bioluminescent imaging (BLI) was performed using an IVIS Spectrum Imaging System (Perkin Elmer, Waltham, MA). Imaging took place 10 minutes after a 200 µL solution of D-luciferin (12.5 mg/mL) was interperitoneally administered. BLI imaging was conducted every 2-5 days until the terminal point of the study. At the terminal point, if required by the study, lungs, liver, spleen and tumors were collected for either immunohistochemistry or flow cytometry analysis.

2.5 Flow cytometry. Anti-mouse antibodies including, CD45 (30-F11), CD11c (HL3), F4/80 (T45-2342), CD11b (M1/70), Ly6G (1A8), Ly6C (AL-21), CD49b (DX5), CD3e (145-2C11), CD8a (53-6.7) and CD4 (GK1.5), were purchased from BD Biosciences and Biolegend with a dye-conjugate for flow cytometry. Flow cytometry analysis was performed 24 h after a fluorescently labeled nanoparticle or the last treatment was administered. Blood was collected via retro-orbital bleeding. Mice were subsequently euthanized, and the tumor, liver, lungs and spleen were removed. Tumors and lungs were digested for 1hr in 1mg/mL collagenase in serum free RPMI medium (Sigma Aldrich/Thermo Fischer Scientific). Organs were gently homogenized and passed through a 70 µm filter to obtain a single cell suspension. Lungs, liver and blood single cell suspensions were washed with ACK lysis buffer (Gibco). Resultant. Single cell suspensions were blocked with anti-mouse CD16/CD32 (2.4G2; BD Biosciences) and stained with the dye-conjugate antibodies and then counterstained with DAPI (BD Biosciences). Fluorescently tagged samples were read on a BD LSR II flow cytometer. Flowjo software was used to analyze and quantify immune cells with the respective markers.

2.6 Evaluation in primary splenocytes. Spleens from healthy BALBc/J mice were harvested. They were homogenized and passed through 70um filters. ACK lysis buffer was used to eliminate any remaining red blood cells. 6 million cells in 1.5mL of DMEM media per well were plated in 24 well plates in serum free

DMEM media. cdGMP loaded mPEG liposomes were incubated with splenocytes in the 24 well plate at a concentration of 20 μg cdGMP/mL of cells in DMEM media. The same was done for c(RGDfC), CDAEWVDVS, and CREKA targeted liposomes. Each targeted liposome was tested in triplicate. They were incubated together at 37 ºC for 24 hours. The supernatant was collected for IFN-B ELISAs (LumiKine Xpress Bioluminescent Cytokine ELISA Kit, Invivogen). The cells were harvested by removing excess supernatant after collection for ELISAs and resuspending the cells in 600uL of media. The cells were then analyzed via flow cytometry as previously described for $CD45^-/CD11c^+$ dendritic cells and $CD45^+/F4/80^+$ macrophages, with M1 macrophages ($CD80^+$) and M2 macrophages ($CD206^+$) subset, all with the additional marker of CD86 (GL-1) from BioLegend.

2.7 Histological staining and microscopy. Immunohistochemistry was conducted to identify the tumor burden in visceral organs and the topological distribution of the targeted nanoparticles within tumor associated microenvironments. Briefly, 4T1 bearing-mice were intravenously injected with fluorescently labeled nanoparticles 24 h prior to organ resection. Mice were anesthetized with a 5% isoflurane inhalant and transcardially perfused with heparinized PBS followed by a 4% paraformaldehyde solution in PBS. The solid mammary tumor, lungs and liver were harvested and placed in 4% paraformaldehyde for 24hrs and then dried in a 30% sucrose (w/v) in PBS solution for 48hrs. Resulting tissues were embedded and frozen in optimum cutting temperature (Thermo Fisher Scientific). Frozen tissue blocks were sliced into 10 μm sections and mounted on gold plated tissue slides. Resultant tissues were counterstained with a DAPI mounting medium (Vector Laboratories). Tissue sections were imaged at 10x and 20x magnification using either a Zeiss Axio Observer Z1 inverted fluorescent microscope or a Leica TCS SP8 gated STED confocal microscope. Larger montages were collected using the automatic tiling via the Mosaic acquisition feature with the associated software.

2.8 Statistical analysis. All statistical analysis was executed using Prism 7 (GraphPad Software). The data depicted was analyzed using a one- or two-way ANOVA with either a post hoc Tukey or Sidak's test; the statistical analysis used is described in each figure legend. Statistical significance is determined by a P-value less than 0.05. Unless mentioned, all values are reported as mean ± SE.

3 Results and discussion

3.1 Characterization of nanoparticles. We developed a 60-nm nanoparticle comprised of a lipid matrix containing DPPC, DOPC, and DSPE-PEG-ligand. DiR' was added to the lipid matrix as a fluorescent reporter for flow cytometry analysis. Nanoparticle variants included fibronectin-targeting nanoparticles (CREKA-NP), $\alpha_v\beta_3$ integrin-targeting nanoparticles (cRGD-NP), P-selectin-targeting nanoparticles (PSN-NP) and untargeted nanoparticles (mPEG-NP). We employed commonly used peptides including the $\alpha_v\beta_3$ integrin-targeting c(RGDfC),[21, 22, 24, 25, 42] the P-selectin-targeting CDAEWVDVS,[22, 23, 25] and the fibronectin-targeting CREKA.[22, 23, 25] Using standard sulfo-SMCC chemistry to conjugate the peptides on the distal end of PEG-amines on the nanoparticle's surface, the ligand density was determined to be approximately 2,000 peptides per particle across all formulations (Bio-Rad Protein Assay).[22, 25] All nanoparticle formulations had nearly identical size (about 47 ± 21 nm) and zeta potential (about -24 ± 14 mV) as shown in Fig. 2A,B. A detailed characterization of the targeted formulations can be found in previous work.[22, 25] All formulations were efficiently and stably loaded with similar amounts of the STING agonist cdGMP (Fig. 2C). The function of the NP variants was evaluated in vitro using RAW 264.7 macrophages and primary splenic cell cultures from BALBc/J mice. First, ELISA analysis showed that the mPEG-NP resulted in a nearly 10-fold increase in the production of the proinflammatory cytokine IFNβ than the free dcGMP (Fig. 2E). In previous work, we have shown free cdGMP cannot efficiently gain access into phagocytic cells leading to negligible production of IFNβ.[14, 43-45] In primary splenocytes, all 4 NP variants produced similarly high levels of IFNβ (Fig. 2E).

Using flow cytometry, quantification of the NP uptake by splenocytes showed that RGD-NP had the highest uptake followed by the CREKA-NP variant (Fig. 2F). Importantly, all formulations exhibited a significant uptake by DCs (Fig. 2G). All NP variants were taken up by at least 50% of DCs. In terms of activation, 65% of $CD11c^+$ DCs were expressing CD80, CD86, or both activation markers after the mPEG-NP treatment (Fig. 2H). The 3 targeted NP variants caused at least 85% of $CD11c^+$ DC to express CD80, CD86, or both markers. Considering the uptake of the targeted nanoparticle variants by splenic DCs exhibited insignificant differences, the observed variability in the activation markers may be attributed to potential additional activation by the targeting ligand or targeted receptor. Notably, the RGD-NP and PSN-

NP formulations strongly activated CD11c$^+$ DCs with 64 and 75% of DCs being double-positive for CD80$^+$ and CD86$^+$.

Fig. 2. *Characterization of nanoparticles. (A) DLS measurement of nanoparticle size. (B) Zeta potential of nanoparticles. (C) Measurements of the loading of the STING agonist cdGMP in the different nanoparticle formulations. Analysis by ELISA for in vitro production of IFNβ in (D) RAW 264.7 macrophages and (E) primary splenocytes. Analysis by flow cytometry of the ex vivo uptake of NPs by (F) primary splenocytes and (G) primary splenic DCs. (H) Analysis by flow cytometry of the activation markers CD80 and CD86 in primary splenic CDllc DCs. Experiments were performed in n=3-5 with statistics by 1-way ANOVA with a post hoc Tukey or Sidak's test (ns: not significant, *P<0.05, **P<0.01, ***P<0.001, ****P<0.0001).*

3.2 Characterization of tumor model. The 4T1 murine model is a standard model to study metastatic breast cancer in immunocompetent mice. The 4T1 cells were orthotopically inoculated into the no.9 inguinal mammary fat pad. As time progressed, the model developed spontaneous metastasis in visceral organs including the lungs and liver reminiscent of the disease observed in human patients.[22, 25, 46] The 4T1 cells were transfected with a lentivirus to stably express cytosolic firefly luciferase and GFP for in vivo and ex vivo cell tracking. After the primary tumor was established, it was surgically removed, so that metastatic foci remained intact and metastatic disease could be studied at early or later stages. Representative BLI images (Fig. 3A) and quantification of BLI signal from the primary site (Fig. 3B) and thoracic region (Fig. 3C) indicate the progression of disease. Using flow cytometry, the 4T1 cancer cells and CD45$^+$ leukocytes were quantified in the primary tumor and lungs 10 days after tumor inoculation. First, it is important to highlight that the immune cells were the dominant cell subpopulation in the primary tumor site, with the leukocyte to tumor cell ratio being about 3:1 (Fig. 3D). Second, the early spread of the disease was observed in both liver and lungs (Fig. 3E,F). To establish the late-stage metastatic setting, the primary tumor was surgically resected on day 14. Analysis on day 23 indicated that metastatic disease progressed rapidly with the content of tumor cells doubling in the liver and lungs between days 10 and 23. Representative histological images show the difference of metastatic spread in the liver and lungs between days 10 and 23 (Fig. 3G).

Fig. 3. *Characterization of mouse tumor model using bioluminescence imaging, flow cytometry and histology. (A) Representative BLI images show an orthotopic 4T1 tumor in mice and its progression overtime. After surgical resection of the primary tumor 14 days after inoculation, metastatic outgrowth and recurrence is observed in the thoracic and abdominal regions. Quantification of the BLI signal from (B) the primary tumor and (C) thoracic region is shown, respectively (n=5). The 4T1 cancer cells (GFP reporter) and CD45+ leukocytes were quantified using flow cytometry in the (D) primary tumor, (E) liver and (F) lungs. (G) Histological evaluation depicts the progression of metastatic disease in the liver and lungs (20x magnification; scale bar = 100 μm; blue: nuclear stain; green:4T1 cancer cells). Mean ± SEM are plotted with statistics by one-/two-way ANOVA with a post hoc Tukey or Sidak's test. **P<0.01; ***P<0.001; ****P<0.0001.*

3.3 Uptake of nanoparticle targeting variants by APCs in different tumor microenvironments. We assessed the in vivo microdistribution and cell uptake of the 4 nanoparticle variants in three different tumor microenvironments, the primary tumor, early metastasis, and late metastasis (Fig. 4A). The nanoparticle variants were intravenously injected at an equal dose ($1x10^{13}$ nanoparticles per mouse) and organs were analyzed by flow cytometry 24 h after injection. Histological analysis showed that NPs deposited throughout the primary tumor (Fig. S1A in Supplementary Information). Most notably, the deposition of NPs in lungs and liver was significant in regions of metastasis compared to minimal accumulation in the healthy portions of these organs (Fig. S1B,C). It has been shown that the nanoparticle variants target biomarkers associated with metastatic sites in the liver and lungs.[22, 24, 25] In the primary tumor, the vast majority of NPs for all the targeting variants was taken up by $CD45^+$ leukocytes ranging from 3- to 11-fold higher than cancer cells (Fig. 4B). Notably, the highest uptake by $CD45^+$ leukocytes was observed for the untargeted NP variant. Specifically, for APCs, the untargeted NP exhibited the highest uptake by both DCs and macrophages (Fig. 4C). In the case of early stage metastasis, integrin-targeting NPs had the highest uptake by lung DCs and macrophages as well as liver macrophages (Fig. 4D,E). It was also observed that, integrin-targeting NPs had the highest uptake by APCs in the blood and the spleen (Fig. S2A-C in Supplementary Information). In the case of late stage metastasis, the untargeted NP was the best overall performer in terms of uptake by APCs in lungs and liver (Fig. 4F,G), which is consistent with a more

advanced TME with a leaky endothelium. All the formulations exhibited similar levels of uptake by APCs NPs were significantly taken up by endothelial cells (Fig. S2F,G).

Fig. 4. *Quantification of nanoparticle uptake by APCs across different TMEs. (A) Timelines show animal modeling, nanoparticle administration and flow cytometry analysis. (B) Flow cytometry analysis of nanoparticle uptake by 4T1 cancer cells and CD45$^+$ leukocytes in primary tumor. Flow cytometry analysis of nanoparticle uptake by CD11c$^+$ dendritic cells and F4/80$^+$ macrophages in (C) primary tumor, (D) lungs at a stage of early metastasis, (E) liver at a stage of early metastasis, (F) lungs at a stage of late metastasis, and (G) liver at a stage of late metastasis (n=5 mice per group). Box and whisker plots (5-95 percentile) with statistics by one-/two-way ANOVA with a post hoc Tukey or Sidak's test. *P<0.05; **P<0.01; ***P<0.001; ****P<0.0001.*

Here, we show that systemic delivery ensured delivery of nanoparticles to the APC-rich perivascular regions of breast cancer in different TMEs. Nanoparticles could passively drain and accumulate into the perivascular niche of TMEs due to the irregular growth of tumor-associated angiogenic blood vessels. The untargeted mPEG-NPs were the main beneficiary of the natural drainage through the leaky endothelium that occurs in an advanced primary tumor due to their relatively high circulation time. This led to the predominant uptake of immunostimulatory NPs by the desired subset of immune cells in primary tumors. On the other hand, targeted NPs were able to seamlessly access APCs in sites of metastasis. In particular, integrin-targeting cRGD-NPs displayed significant APC accumulation in sites of early metastasis that exhibit the onset of a developing remodeled endothelium. However, the untargeted mPEG-NPs showed higher uptake by APCs than the targeted NP variants in sites of late metastasis. This could be attributed to the fact the late-stage metastasis transitions from a developing remodeled endothelium to a leaky endothelium similar to a primary tumor mass. Overall, this study is in good agreement to previous studies indicating that systemic delivery of NPs is the ideal route to efficiently access micrometastasis.[21-25, 42, 47-50] In previous studies,[51-63] we exploited various targeting ligands to direct nanoparticles to metastatic breast cancers. While these are common targeting ligands used to deliver anticancer drugs to tumors, we show that these ligands can further increase the uptake of NPs by immune cells in different landscapes of the TME. Considering the unique features and dynamic nature of the TME,

the different variants of the targeted immunostimulatory NPs resulted in variable uptake by immune cell subsets depending on the location and stage of the TME (e.g., primary tumor, early or late metastasis in liver or lungs). Future work can expand on testing more specialized targeting ligands for improved binding and enhanced uptake of immunostimulatory NPs by APCs including chemokine receptors CCR2, mannose, and ICAM-1.[64-68]

3.4 Evaluation of cellular response to immunostimulatory NP treatment. Based on the findings of the cell uptake studies, we selected to evaluate the antitumor immune response of the untargeted NP and integrin-targeting NP, since these were the overall best performers in primary tumors and early metastasis, respectively. The two formulations (i.e., cRGD-NP and mPEG- NP) exhibited stable and similar loading of the agonist (Fig. S3A in Supplementary Information). Mice bearing mammary 4T1 tumors were treated on day 8 with a single dose of untargeted NP or integrin-targeting NP at a dose of 10 μg of cdGMP per mouse (Fig. 5A). At the start of treatment, the tumor volume was about 100 mm^3. On day 10, organs were resected and analyzed for immune cell content to evaluate the cellular response to the immunostimulatory NP treatment 48 h after intravenous administration. Specifically, we focused on the primary tumor and organs prone to metastasis, such as lungs and liver. BLI indicated the immunostimulatory NP treatments produced a decrease of the tumor burden in both the primary tumor site and the thoracic cavity when compared to an untreated control (Fig. 5B,D). Further, both treatments resulted in a significantly lower primary tumor volume than the untreated control (Fig. 5E). It should be noted that the bulk of the tumor mass was reduced by one third in the case of the untargeted NP (Fig. S3B). In the primary tumor, the untargeted NPs produced a significantly higher increase of DCs and natural killer (NK) cells than the integrin-targeting NPs (Fig. 5F). Similarly, untargeted NPs had superior results in the lungs achieving significant elevation of DCs, macrophages and NK cells (Fig. 5G). Considering the early-stage metastasis on day 10, the integrin-targeting NPs outperformed the untargeted NPs in the liver (Fig. 5H). Further, the integrin-targeting NPs caused a significant increase of NK cells in the blood (Fig. S3C). On the other hand, untargeted NPs caused significant elevation of macrophages in the spleen in the case of (Fig. S3D). Besides innate immune cells, $CD4^+$ T cells were significantly elevated in the primary tumor and lungs for both NP

treatments (Fig. S3E,F) and in the blood for the integrin-targeting NPs (Fig. S3H). Due to the short time scale of the study, no significant changes in $CD8^+$ T cells were observed in any organ 48 h after the immunostimulatory NP treatments (Fig. S3E-I).

Fig. 5. *Mechanistic study of the cellular immune response to immunostimulatory NPs 48 h after systemic delivery. (A) Timeline shows the treatment regimen. The untargeted or $\alpha_v\beta_3$ integrin-targeting immunostimulatory NP variants were loaded with the STING agonist cdGMP. Flow cytometry analysis was performed 48 h after intravenous administration of the formulations at 10 μg cdGMP per mouse. (B) Representative BLI images show the progression of the disease. Quantification of the BLI signal is shown for (C) the primary tumor and (D) lungs. Black arrow indicated the treatment day. (E) Primary tumor volume was obtained using caliper measurements at the terminal point on day 10. Flow cytometry analysis of innate immune cell recruitment to the (F) primary tumor, (G) lungs, and (H) liver 48 h after administration of formulations. N=5 mice per condition. Box and whisker plots (5-95 percentile) both with statistics by one-/two-way ANOVA with a post hoc Tukey or Sidak's test. *P<0.05; **P<0.01; ***P<0.001; ****P<0.0001.*

Compared to the findings of the uptake of the various NP variants, the cellular response to the immunostimulatory nanoparticles and the innate immune cell recruitment into the tumor detailed a slightly different story. As expected, mPEG -NP induced increases in DCs, macrophages, and NK cells within the primary tumor. However, this formulation also showed extensive recruitment in the lungs where, based on the uptake studies, we expected the integrin-targeting NP to outperform the untargeted formulation. A potential explanation may be that the cancer cell content and antigen payload within the solid tumor microenvironment is significantly greater than that available to APCs at metastatic sites. The reactivation and subsequent migration of innate immune cell within the solid tumor can potentially explain why APC recruitment was greater for the untargeted immuno-nanoparticle not only in the tumor but also within the lungs. Integrin-targeting, however, outperformed the untargeted formulation in the liver. This can be corroborated by APC uptake and the near 3-fold deposition within activated endothelial cells which are also shown to have STING machinery.[36] The broad recruitment by the untreated formulation in the tumor and the lungs, further exemplifies their outstanding survival and slowed rechallenge tumor outgrowth.

3.5 Long-term therapeutic efficacy. The long-term therapeutic efficacy of the untargeted and integrin-targeting immunostimulatory NPs was evaluated in a neoadjuvant scenario. The treatment scheme involved untargeted or integrin-targeting immunostimulatory NP, surgical resection of primary tumor and the checkpoint inhibitor anti-PD1. Prior to surgical resection on day 8, mice were treated with two consecutive doses of immunostimulatory NPs on day 6 and 7 (Fig. 6A). After surgical resection, two consecutive doses of immunostimulatory NPs were administered in combination with anti-PD1 on day 12 and 13. The treatment conditions included the following groups: 1) untreated, 2) anti-PD1, 3) untargeted NP (before surgery - 1x) + anti-PD1, 4) untargeted NP (before and after surgery - 2x) + anti-PD1, and 5) integrin-targeting NP (before and after surgery - 2x) + anti-PD1. Representative BLI images show the positive long-term outcomes of the immuno-stimulatory NP treatments (Fig. 6B). Peripheral $CD8^+$ T cells in the blood provides a measure to evaluate activation of APCs in the TME and subsequent priming of effector T cells. In particular, the untargeted NP treatments in combination with anti-PD1 resulted in significant elevation of $CD8^+$ T cells in the blood (Fig. 6C). The treatment scheme consisting of untargeted NP treatments before and after surgery outperformed all treatment schemes producing a remarkable increase of $CD8^+$ T cells in the blood on day 21. Increases were also observed for macrophages, NK cells and $CD4^+$ T cells in the blood mostly for the treatment schemes involving the untargeted NP (Fig. S4A-D in Supplementary Information). Based on caliper measurements of tumor recurrence in the abdominal area, only the treatment schemes that included the untargeted NP treatments, either before surgery or both before and after surgery, produced a complete response with no measurable tumor in the abdominal area (Fig. 6D). While 100% of the untreated group and the anti-PD1-treated group did not survive, the treatment scheme that included untargeted NP before and after surgery showed the highest survival with more than 85% of this group showing no sign of the disease 2 months after the initial tumor inoculation (Fig. 6E). The survival data are in good agreement with the BLI signal from the lungs and abdominal region indicating that no metastatic disease was observed in the majority of the two groups treated with untargeted NP (Fig. 6F,G). These mice from these two groups with BLI signal below the background baseline were considered good responders and were included in subsequent studies assessing antitumor immunologic

memory. The good responders from the two groups that received untargeted NP (n=4 for each group) were subjected to a tumor rechallenge by the inoculation of $1x10^5$ cancer cells in the flank of the animals, a fifth of the original inoculant cell count. Both groups exhibited a significant increase in survival and decrease in tumor burden when compared to a naïve control group (Fig. 7A,B). However, the group that was treated with untargeted NP before and after surgery outperformed the group that received the NP treatment only before surgery. It is important to note that the rechallenge mice were not re-treated indicating the likelihood of a T-cell memory response associated with the increase in mean survival when comparing them to the naïve control. In further studies, we aim to characterize this response by analyzing $CD8^+$ $CD69^+$ T-cells both in the blood and within tumor niches.

Fig. 6. *Long-term efficacy of immunostimulatory NPs in combination with surgery and anti-PD1. (A) Timeline shows animal modeling, treatment schedule and related analysis. The immunostimulatory NP treatment included the untargeted NP or the integrin-targeting NP. The immunostimulatory NPs were administered on day 6 and 7 at a dose of 10 μg of cdGMP per mouse, followed by surgical resection on day 8. Some groups received a second immunostimulatory NPs (10 μg of cdGMP per mouse) on day 12 and 13 coupled with a subcutaneous administration of anti-PD1 (250 μg). (B) Representative BLI images show the progression of disease for some conditions. (C) The $CD8^+$ T-cells in the blood was measured on day 14 and 21 using flow cytometry. (D) Caliper measurement of tumor recurrence was performed in the abdominal area. (E) Kaplan-Meier survival analysis. Quantification of BLI signal is shown for the (F) abdominal and (G) thoracic regions (top panels). The two groups that contained the untargeted NP treatment were further stratified into good and poor responders using the background BLI level (106 photons/second) as a threshold. N=7 mice per condition. Mean ± SEM are plotted with statistics by one-/two-way ANOVA with a post hoc Tukey or Sidak's test. *P<0.05; **P<0.01; ***P<0.001; ****P<0.0001.*

Fig. 7. *Response of good responders to a tumor rechallenge. The treatment scheme of animals bearing 4T1 tumors included surgical resection of the primary tumor, anti-PD1 and untargeted immunostimulatory NP before and after surgery, indicated as mPEG-NP(x2), or only before surgery indicated as mPEG-NP(x1). The good responders from the two groups were rechallenged 42 days after the initial inoculation with $1x10^5$ 4T1 cells on their right flank. (A) Caliper measurement of the flank tumor size. (B) Kaplan-Meier survival analysis. N=4 mice per condition. Box and*

*whisker plots (5-95 percentile) both with statistics by one-/two-way ANOVA with a post hoc Tukey or Sidak's test. **P<0.01.*

4 Conclusion

Harnessing the innate immune system using immunostimulatory NPs has the potential to improve tumor response to existing immunotherapies, such as immune checkpoint inhibitors (CPIs), which can bring transformative treatments for high-risk breast cancer patients. By activating innate immunity within the TME, the immunity cycle can be restored allowing for the necessary communication between innate and adaptive immune cells. Importantly, activated tumor-resident APCs are capable of directly processing tumor-associated antigens shed from cancer cells in the TME. In this work, we modeled neoadjuvant therapy using the immunostimulatory NPs in combination with the anti-PD1 checkpoint inhibitor by surgically removing the primary tumor. STING and IFNβ-dependent antitumor immunity has shown to trigger production of immune checkpoint proteins (PD1, IDO, CTLA-4) that cause immune resistance.[13, 69, 70] This made the combination of the immunostimulatory NPs with anti-PD1 highly synergistic resulting in amplification of T cell response and ultimately cure of 90% of mice. Our studies indicate that the untargeted immunostimulatory NP was sufficient to produce remarkable therapeutic outcomes in a neoadjuvant setting. In the future, we will explore whether targeted immunostimulatory NP are more effective in a purely metastatic setting.

In conclusion, we evaluated the ability of common tumor-targeting schemes to direct immunostimulatory NPs into the tumor immune microenvironment of metastatic breast cancer. We identified that the untargeted NP had the highest uptake by APCs in the primary tumor and late-stage metastasis, whereas the integrin-targeting NP variant was superior in sites of early metastasis. Using a STING agonist as the nanoparticle's cargo, successful trafficking of NPs in the perivascular TME resulted in activation and expansion of APCs in sites of the primary tumor as well as early and late metastasis. Notably, the highest increase of immune cell infiltration was observed for the untargeted NPs as their uptake by APCs in the primary tumor was approximately 3 fold higher than that of the targeting NP variants. Considering the significant expansion of APCs and the tumor-associated antigens in the TME, long-term

studies showed continuously increasing peripheral $CD8^+$ T cells. In combination with anti-PD1 treatment to boost the activity of $CD8^+$ T cells, the majority of the treated group were cancer-free and exhibited long-lasting antitumor capacity.

Acknowledgements

This work was supported by grants from the NCI (U01CA198892, R01CA253627), the Case Comprehensive Cancer Center Support Grant (P30CA043703) and the Shiverick Family Fund, the Clinical Translational Science Collaborative of Cleveland (UL1TR002548), and the Alex's Lemonade Stand Foundation (to E. Karathanasis). G. Covarrubias, T Moon and M. Lorkowski were supported by fellowships from the NIH Interdisciplinary Biomedical Imaging Training Program (T32EB007509) administered by the Department of Biomedical Engineering, Case Western Reserve University. P.A. Bielecki was supported by a graduate research fellowship from the National Science Foundation.

References

1. S. Meng, D. Tripathy, E. P. Frenkel, S. Shete, E. Z. Naftalis, J. F. Huth, P. D. Beitsch, M. Leitch, S. Hoover, D. Euhus, B. Haley, L. Morrison, T. P. Fleming, D. Herlyn, L. W. Terstappen, T. Fehm, T. F. Tucker, N. Lane, J. Wang and J. W. Uhr, *Clin Cancer Res*, 2004, **10**, 8152-8162.
2. C. A. Klein, *Curr Opin Genet Dev*, 2011, **21**, 42-49.
3. S. A. Eccles, E. O. Aboagye, S. Ali, A. S. Anderson, J. Armes, F. Berditchevski, J. P. Blaydes, K. Brennan, N. J. Brown, H. E. Bryant, N. J. Bundred, J. M. Burchell, A. M. Campbell, J. S. Carroll, R. B. Clarke, C. E. Coles, G. J. Cook, A. Cox, N. J. Curtin, L. V. Dekker, S. Silva Idos, S. W. Duffy, D. F. Easton, D. M. Eccles, D. R. Edwards, J. Edwards, D. Evans, D. F. Fenlon, J. M. Flanagan, C. Foster, W. M. Gallagher, M. Garcia-Closas, J. M. Gee, A. J. Gescher, V. Goh, A. M. Groves, A. J. Harvey, M. Harvie, B. T. Hennessy, S. Hiscox, I. Holen, S. J. Howell, A. Howell, G. Hubbard, N. Hulbert-Williams, M. S. Hunter, B. Jasani, L. J. Jones, T. J. Key, C. C. Kirwan, A. Kong, I. H. Kunkler, S. P. Langdon, M. O. Leach, D. J. Mann, J. F. Marshall, L. Martin, S. G. Martin, J. E. Macdougall, D. W. Miles, W. R. Miller, J. R. Morris, S. M. Moss, P. Mullan, R. Natrajan, J. P. O'Connor, R.

O'Connor, C. Palmieri, P. D. Pharoah, E. A. Rakha, E. Reed, S. P. Robinson, E. Sahai, J. M. Saxton, P. Schmid, M. J. Smalley, V. Speirs, R. Stein, J. Stingl, C. H. Streuli, A. N. Tutt, G. Velikova, R. A. Walker, C. J. Watson, K. J. Williams, L. S. Young and A. M. Thompson, *Breast Cancer Res*, 2013, **15**, R92.

4. R. L. Siegel, K. D. Miller and A. Jemal, *CA Cancer J Clin*, 2018, **68**, 7-30.
5. R. D. Schreiber, L. J. Old and M. J. Smyth, *Science*, 2011, **331**, 1565-1570.
6. L. Borriello, R. C. Seeger, S. Asgharzadeh and Y. A. DeClerck, *Cancer Lett*, 2016, **380**, 304-314.
7. J. A. Joyce and D. T. Fearon, *Science*, 2015, **348**, 74-80.
8. L. Muller, P. Aigner and D. Stoiber, *Front Immunol*, 2017, **8**, 304.
9. M. A. Swartz, S. Hirosue and J. A. Hubbell, *Sci Transl Med*, 2012, **4**, 148rv149.
10. M. Banys, A. D. Hartkopf, N. Krawczyk, T. Kaiser, F. Meier-Stiegen, T. Fehm and H. Neubauer, *Breast cancer*, 2012, **4**, 183-191.
11. C. M. Ghajar, *Nat Rev Cancer*, 2015, **15**, 238-247.
12. D. Shae, K. W. Becker, P. Christov, D. S. Yun, A. K. R. Lytton-Jean, S. Sevimli, M. Ascano, M. Kelley, D. B. Johnson, J. M. Balko and J. T. Wilson, *Nat Nanotechnol*, 2019, **14**, 269-278.
13. N. Cheng, R. Watkins-Schulz, R. D. Junkins, C. N. David, B. M. Johnson, S. A. Montgomery, K. J. Peine, D. B. Darr, H. Yuan, K. P. McKinnon, Q. Liu, L. Miao, L. Huang, E. M. Bachelder, K. M. Ainslie and J. P. Ting, *JCI Insight*, 2018, **3**.
14. P. U. Atukorale, S. P. Raghunathan, V. Raguveery, C. Zheng, T. J. Moon, M. L. Weiss, P. A. Bielecki, A. L. Goldberg, G. Covarrubias, C. J. Hoimes and E. Karathanasis, *Cancer Research*, 2019, **79** 5394-5406
15. L. Corrales, L. H. Glickman, S. M. McWhirter, D. B. Kanne, K. E. Sivick, G. E. Katibah, S. R. Woo, E. Lemmens, T. Banda, J. J. Leong, K. Metchette, T. W. Dubensky, Jr. and T. F. Gajewski, *Cell Rep*, 2015, **11**, 1018-1030.
16. L. Corrales and T. F. Gajewski, *Clinical cancer research : an official journal of the American Association for Cancer Research*, 2015, **21**, 4774-4779.
17. L. Corrales and T. F. Gajewski, *Cytokine*, 2016, **77**, 245-247.

18. L. Corrales, S. M. McWhirter, T. W. Dubensky, Jr. and T. F. Gajewski, *The Journal of clinical investigation*, 2016, **126**, 2404-2411.

19. S. R. Woo, M. B. Fuertes, L. Corrales, S. Spranger, M. J. Furdyna, M. Y. Leung, R. Duggan, Y. Wang, G. N. Barber, K. A. Fitzgerald, M. L. Alegre and T. F. Gajewski, *Immunity*, 2014, **41**, 830-842.

20. O. Turan, P. Bielecki, K. Tong, G. Covarrubias, T. Moon, A. Rahmy, S. Cooley, Y. Park, P. M. Peiris, K. B. Ghaghada and E. Karathanasis, *Mol Pharm*, 2019, **16**, 4352-4360.

21. G. Covarrubias, F. He, S. Raghunathan, O. Turan, P. M. Peiris, W. P. Schiemann and E. Karathanasis, *PLoS One*, 2019, **14**, e0220474.

22. P. M. Peiris, F. He, G. Covarrubias, S. Raghunathan, O. Turan, M. Lorkowski, B. Gnanasambandam, C. Wu, W. P. Schiemann and E. Karathanasis, *Nanoscale*, 2018, **10**, 6861-6871.

23. G. Covarrubias, A. Cha, A. Rahmy, M. Lorkowski, V. Perera, B. O. Erokwu, C. Flask, P. M. Peiris, W. P. Schiemann and E. Karathanasis, *PLoS One*, 2018, **13**, e0204296.

24. P. M. Peiris, P. Deb, E. Doolittle, G. Doron, A. Goldberg, P. Govender, S. Shah, S. Rao, S. Carbone, T. Cotey, M. Sylvestre, S. Singh, W. P. Schiemann, Z. Lee and E. Karathanasis, *J Pharm Sci*, 2015, **104**, 2600-2610.

25. E. Doolittle, P. M. Peiris, G. Doron, A. Goldberg, S. Tucci, S. Rao, S. Shah, M. Sylvestre, P. Govender, O. Turan, Z. Lee, W. P. Schiemann and E. Karathanasis, *ACS Nano*, 2015, **9**, 8012-8021.

26. E. Serres, F. Debarbieux, F. Stanchi, L. Maggiorella, D. Grall, L. Turchi, F. Burel-Vandenbos, D. Figarella-Branger, T. Virolle, G. Rougon and E. Van Obberghen-Schilling, *Oncogene*, 2014, **33**, 3451-3462.

27. T. Ohnishi, S. Hiraga, S. Izumoto, H. Matsumura, Y. Kanemura, N. Arita and T. Hayakawa, *Clin Exp Metastasis*, 1998, **16**, 729-741.

28. D. Neri and R. Bicknell, *Nat Rev Cancer*, 2005, **5**, 436-446.

29. L. Borsi, E. Balza, M. Bestagno, P. Castellani, B. Carnemolla, A. Biro, A. Leprini, J. Sepulveda, O. Burrone, D. Neri and L. Zardi, *Int J Cancer*, 2002, **102**, 75-85.
30. H. Laubli and L. Borsig, *Seminars in cancer biology*, 2010, **20**, 169-177.
31. Y. J. Kim, L. Borsig, H. L. Han, N. M. Varki and A. Varki, *Am J Pathol*, 1999, **155**, 461-472.
32. R. J. Ludwig, B. Boehme, M. Podda, R. Henschler, E. Jager, C. Tandi, W. H. Boehncke, T. M. Zollner, R. Kaufmann and J. Gille, *Cancer Res*, 2004, **64**, 2743-2750.
33. M. L. Nierodzik and S. Karpatkin, *Cancer Cell*, 2006, **10**, 355-362.
34. L. Borsig, R. Wong, J. Feramisco, D. R. Nadeau, N. M. Varki and A. Varki, *Proc Natl Acad Sci U S A*, 2001, **98**, 3352-3357.
35. S. A. Mousa and L. J. Petersen, *Thromb Haemost*, 2009, **102**, 258-267.
36. O. Demaria, A. De Gassart, S. Coso, N. Gestermann, J. Di Domizio, L. Flatz, O. Gaide, O. Michielin, P. Hwu, T. V. Petrova, F. Martinon, R. L. Modlin, D. E. Speiser and M. Gilliet, *Proc Natl Acad Sci U S A*, 2015, **112**, 15408-15413.
37. H. Yang, W. S. Lee, S. J. Kong, C. G. Kim, J. H. Kim, S. K. Chang, S. Kim, G. Kim, H. J. Chon and C. Kim, *J Clin Invest*, 2019, **130**, 4350-4364.
38. L. J. Gay and B. Felding-Habermann, *Nat Rev Cancer*, 2011, **11**, 123-134.
39. A. G. Dupuy and E. Caron, *J Cell Sci*, 2008, **121**, 1773-1783.
40. R. Hanayama, M. Tanaka, K. Miwa, A. Shinohara, A. Iwamatsu and S. Nagata, *Nature*, 2002, **417**, 182-187.
41. J. Savill, I. Dransfield, N. Hogg and C. Haslett, *Nature*, 1990, **343**, 170-173.
42. P. M. Peiris, R. Toy, E. Doolittle, J. Pansky, A. Abramowski, M. Tam, P. Vicente, E. Tran, E. Hayden, A. Camann, A. Mayer, B. O. Erokwu, Z. Berman, D. Wilson, H. Baskaran, C. A. Flask, R. A. Keri and E. Karathanasis, *ACS Nano*, 2012, **6**, 8783-8795.
43. M. E. Lorkowski, P. U. Atukorale, P. A. Bielecki, K. H. Tong, G. Covarrubias, Y. Zhang, G. Loutrianakis, T. J. Moon, A. R. Santulli, W. M. Becicka and E. Karathanasis, *J Control Release*, 2021, **330**, 1095–1105.

44. P. A. Bielecki, M. E. Lorkowski, W. M. Becicka, P. U. Atukorale, T. J. Moon, Y. Zhang, M. Wiese, G. Covarrubias, S. Ravichandran and E. Karathanasis, *Nanoscale Horiz*, 2021, **6**, 156-167.

45. W. M. Becicka, P. A. Bielecki, M. E. Lorkowski, T. J. Moon, Y. Zhang, P. U. Atukorale, K. H. Tong, G. Covarrubias and E. Karathanasis, *Nanoscale Advances*, 2021, **3**, 4961-4972.

46. K. Tao, M. Fang, J. Alroy and G. G. Sahagian, *BMC Cancer*, 2008, **8**, 228.

47. R. Toy, P. M. Peiris, K. B. Ghaghada and E. Karathanasis, *Nanomedicine (Lond)*, 2014, **9**, 121-134.

48. P. M. Peiris, R. Toy, A. Abramowski, P. Vicente, S. Tucci, L. Bauer, A. Mayer, M. Tam, E. Doolittle, J. Pansky, E. Tran, D. Lin, W. P. Schiemann, K. B. Ghaghada, M. A. Griswold and E. Karathanasis, *J Control Release*, 2014, **173**, 51-58.

49. R. Toy, E. Hayden, A. Camann, Z. Berman, P. Vicente, E. Tran, J. Meyers, J. Pansky, P. M. Peiris, H. Wu, A. Exner, D. Wilson, K. B. Ghaghada and E. Karathanasis, *ACS Nano*, 2013, **7**, 3118-3129.

50. P. M. Peiris, R. Toy, A. Abramowski, P. Vicente, S. Tucci, L. Bauer, A. Mayer, M. Tam, E. Doolittle, J. Pansky, E. Tran, W. P. Schiemann, K. B. Ghaghada, M. A. Griswold and E. Karathanasis, *Journal of Controlled Release*, 2013, doi: 10.1016/j.jconrel.2013.1010.1031.

51. M. K. Wendt, M. A. Taylor, B. J. Schiemann and W. P. Schiemann, *Molecular biology of the cell*, 2011, **22**, 2423-2435.

52. C. D. Morrison, J. G. Parvani and W. P. Schiemann, *Cancer Lett*, 2013, DOI: 10.1016/j.canlet.2013.02.048.

53. M. K. Wendt, J. A. Smith and W. P. Schiemann, *Oncogene*, 2010, **29**, 6485-6498.

54. A. J. Gooding, B. Zhang, F. K. Jahanbani, H. L. Gilmore, J. C. Chang, S. Valadkhan and W. P. Schiemann, *Scientific reports*, 2017, **7**, 12698.

55. A. J. Gooding, B. Zhang, L. Gunawardane, A. Beard, S. Valadkhan and W. P. Schiemann, *Oncogene*, 2018, DOI: 10.1038/s41388-018-0586-4.

56. M. K. Wendt, M. Tian and W. P. Schiemann, *Cell and tissue research*, 2012, **347**, 85-101.

57. M. K. Wendt, M. A. Taylor, B. J. Schiemann, K. Sossey-Alaoui and W. P. Schiemann, *Breast Cancer Res*, 2014, **16**, R24.

58. A. J. Gooding and W. P. Schiemann, *Transl Cancer Res*, 2016, **5**, S226-S232.

59. N. J. Robinson and W. P. Schiemann, *Biochim Biophys Acta*, 2016, **1866**, 320-329.

60. A. A. La Belle and W. P. Schiemann, *Cell cycle*, 2017, **16**, 497-498.

61. M. A. Taylor, Y. H. Lee and W. P. Schiemann, *Gene expression*, 2011, **15**, 117-132.

62. M. A. Taylor, K. Sossey-Alaoui, C. L. Thompson, D. Danielpour and W. P. Schiemann, *J Clin Invest*, 2013, **123**, 150-163.

63. M. K. Wendt and W. P. Schiemann, *Breast Cancer Res*, 2009, **11**, R68.

64. C. L. Roland, A. H. Harken, M. G. Sarr and C. C. Barnett, Jr., *Surgery*, 2007, **141**, 705-707.

65. J. Yang, L. Zhang, C. Yu, X. F. Yang and H. Wang, *Biomark Res*, 2014, **2**, 1.

66. A. H. Klimp, E. G. de Vries, G. L. Scherphof and T. Daemen, *Crit Rev Oncol Hematol*, 2002, **44**, 143-161.

67. L. Martinez-Pomares, *J Leukoc Biol*, 2012, **92**, 1177-1186.

68. M. N. Andersen, N. F. Andersen, S. Rodgaard-Hansen, M. Hokland, N. Abildgaard and H. J. Moller, *Leuk Res*, 2015, **39**, 971-975.

69. H. Lemos, E. Mohamed, L. Huang, R. Ou, G. Pacholczyk, A. S. Arbab, D. Munn and A. L. Mellor, *Cancer Res*, 2016, **76**, 2076-2081.

70. W. Xu, J. Dong, Y. Zheng, J. Zhou, Y. Yuan, H. M. Ta, H. E. Miller, M. Olson, K. Rajasekaran, M. S. Ernstoff, D. Wang, S. Malarkannan and L. Wang, *Cancer Immunol Res*, 2019, **7**, 1497-1510.

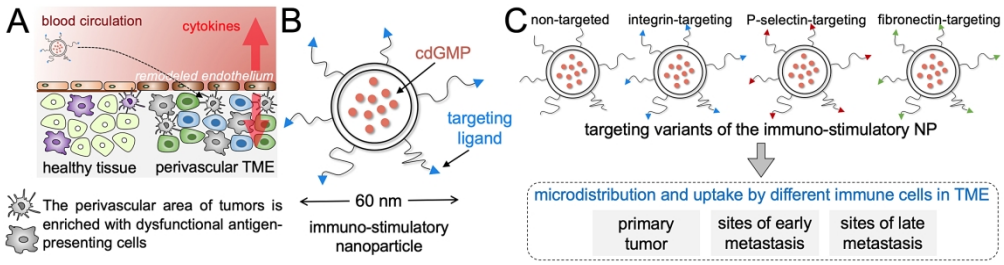

Fig. 1. Illustration of targeting schemes for the delivery of immunostimulatory nanoparticles to tumors. (A) Systemic administration allows immunostimulatory nanoparticles to reach antigen-presenting cells in the near-perivascular area in sites of a primary tumor and metastasis. (B) Illustration of the 60-nm immunostimulatory nanoparticles loaded with a STING agonist (cdGMP). The distal ends of PEG coating can be used to link targeting ligands. (C) Schematic representation shows different immuno-stimulatory nanoparticle variants including untargeted, integrin-targeting, P-selectin-targeting and fibronectin-targeting. The microdistribution and uptake of the nanoparticle variants by different immune cell subsets is evaluated in three different breast cancer landscapes including primary tumor, early metastasis and late metastasis.

254x65mm (300 x 300 DPI)

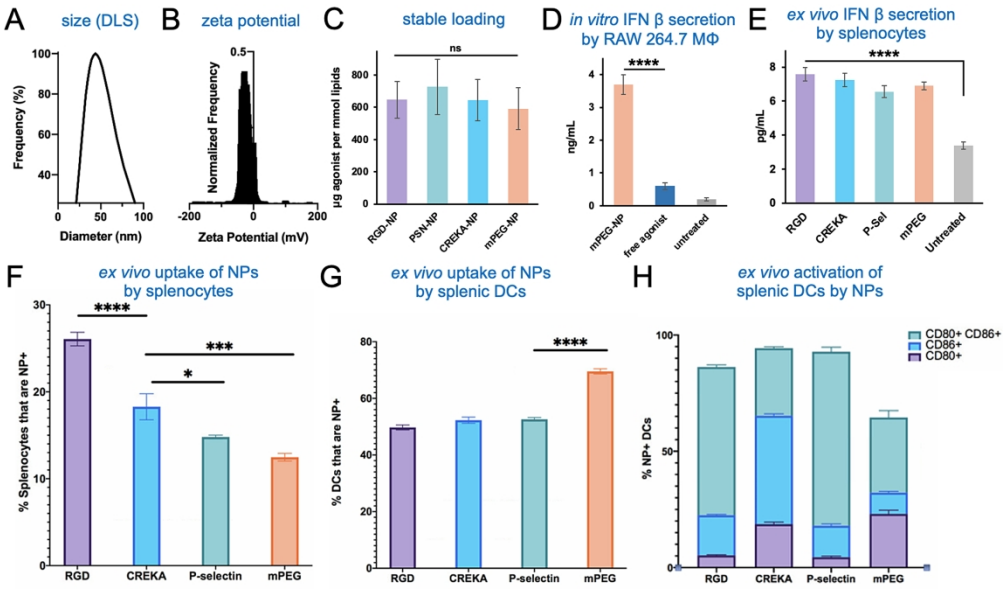

Fig. 2. Characterization of nanoparticles. (A) DLS measurement of nanoparticle size. (B) Zeta potential of nanoparticles. (C) Measurements of the loading of the STING agonist cdGMP in the different nanoparticle formulations. Analysis by ELISA for in vitro production of IFNβ in (D) RAW 264.7 macrophages and (E) primary splenocytes. Analysis by flow cytometry of the ex vivo uptake of NPs by (F) primary splenocytes and (G) primary splenic DCs. (H) Analysis by flow cytometry of the activation markers CD80 and CD86 in primary splenic CDIIc DCs. Experiments were performed in n=3-5 with statistics by 1-way ANOVA with a post hoc Tukey or Sidak's test (ns: not significant, *P<0.05, **P<0.01, ***P<0.001, ****P<0.0001).

228x133mm (300 x 300 DPI)

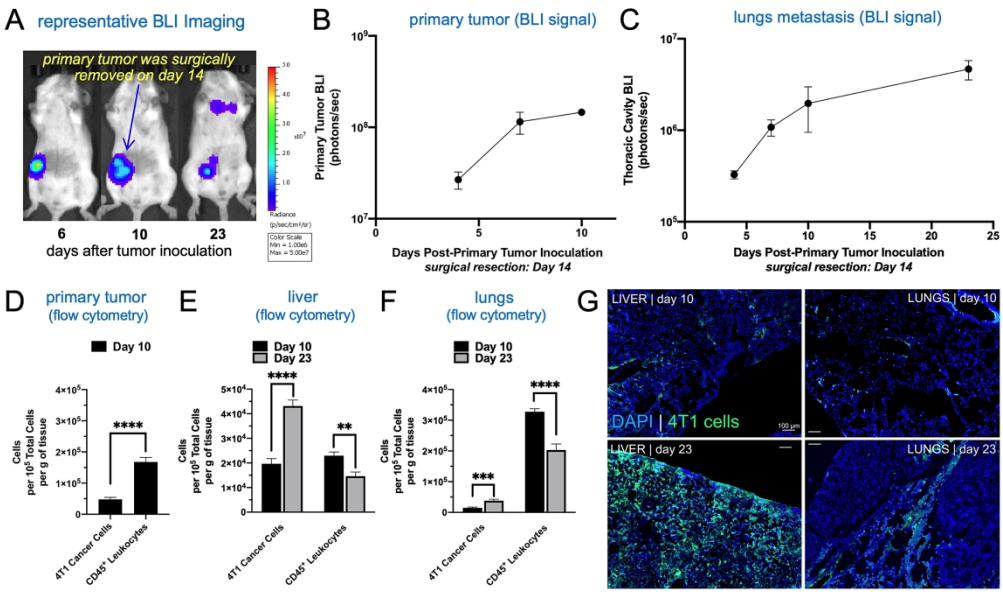

Fig. 3. Characterization of mouse tumor model using bioluminescence imaging, flow cytometry and histology. (A) Representative BLI images show an orthotopic 4T1 tumor in mice and its progression overtime. After surgical resection of the primary tumor 14 days after inoculation, metastatic outgrowth and recurrence is observed in the thoracic and abdominal regions. Quantification of the BLI signal from (B) the primary tumor and (C) thoracic region is shown, respectively (n=5). The 4T1 cancer cells (GFP reporter) and CD45+ leukocytes were quantified using flow cytometry in the (D) primary tumor, (E) liver and (F) lungs. (G) Histological evaluation depicts the progression of metastatic disease in the liver and lungs (20x magnification; scale bar = 100 □m; blue: nuclear stain; green:4T1 cancer cells). Mean □ SEM are plotted with statistics by one-/two-way ANOVA with a post hoc Tukey or Sidak's test. **P<0.01; ***P<0.001; ****P<0.0001.

254x149mm (300 x 300 DPI)

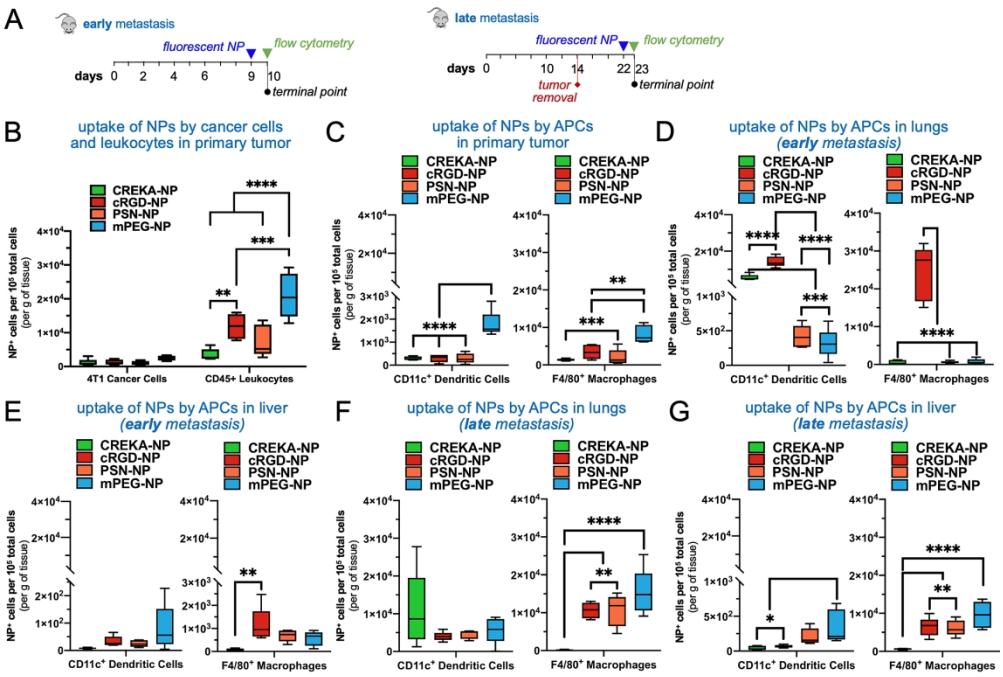

Fig. 4. Quantification of nanoparticle uptake by APCs across different TMEs. (A) Timelines show animal modeling, nanoparticle administration and flow cytometry analysis. (B) Flow cytometry analysis of nanoparticle uptake by 4T1 cancer cells and CD45¬+ leukocytes in primary tumor. Flow cytometry analysis of nanoparticle uptake by CD11c+ dendritic cells and F4/80+ macrophages in (C) primary tumor, (D) lungs at a stage of early metastasis, (E) liver at a stage of early metastasis, (F) lungs at a stage of late metastasis, and (G) liver at a stage of late metastasis (n=5 mice per group). Box and whisker plots (5-95 percentile) with statistics by one-/two-way ANOVA with a post hoc Tukey or Sidak's test. *P<0.05; **P<0.01; ***P<0.001; ****P<0.0001.

254x170mm (300 x 300 DPI)

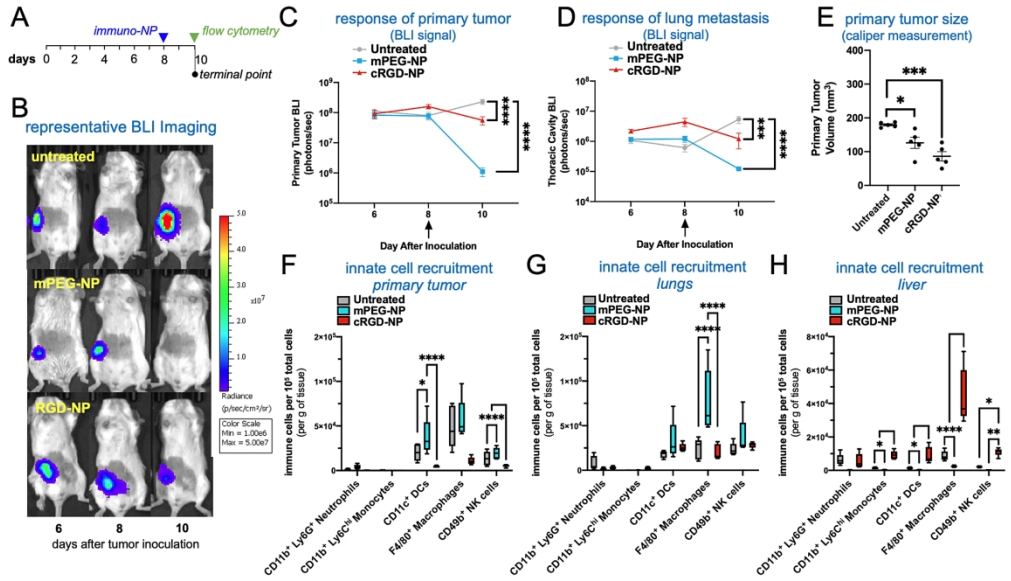

Fig. 5. Mechanistic study of the cellular immune response to immunostimulatory NPs 48 h after systemic delivery. (A) Timeline shows the treatment regimen. The untargeted or αvβ3 integrin-targeting immunostimulatory NP variants were loaded with the STING agonist cdGMP. Flow cytometry analysis was performed 48 h after intravenous administration of the formulations at 10 μg cdGMP per mouse. (B) Representative BLI images show the progression of the disease. Quantification of the BLI signal is shown for (C) the primary tumor and (D) lungs. Black arrow indicated the treatment day. (E) Primary tumor volume was obtained using caliper measurements at the terminal point on day 10. Flow cytometry analysis of innate immune cell recruitment to the (F) primary tumor, (G) lungs, and (H) liver 48 h after administration of formulations. N=5 mice per condition. Box and whisker plots (5-95 percentile) both with statistics by one-/two-way ANOVA with a post hoc Tukey or Sidak's test. *P<0.05; **P<0.01; ***P<0.001; ****P<0.0001.

228x131mm (300 x 300 DPI)

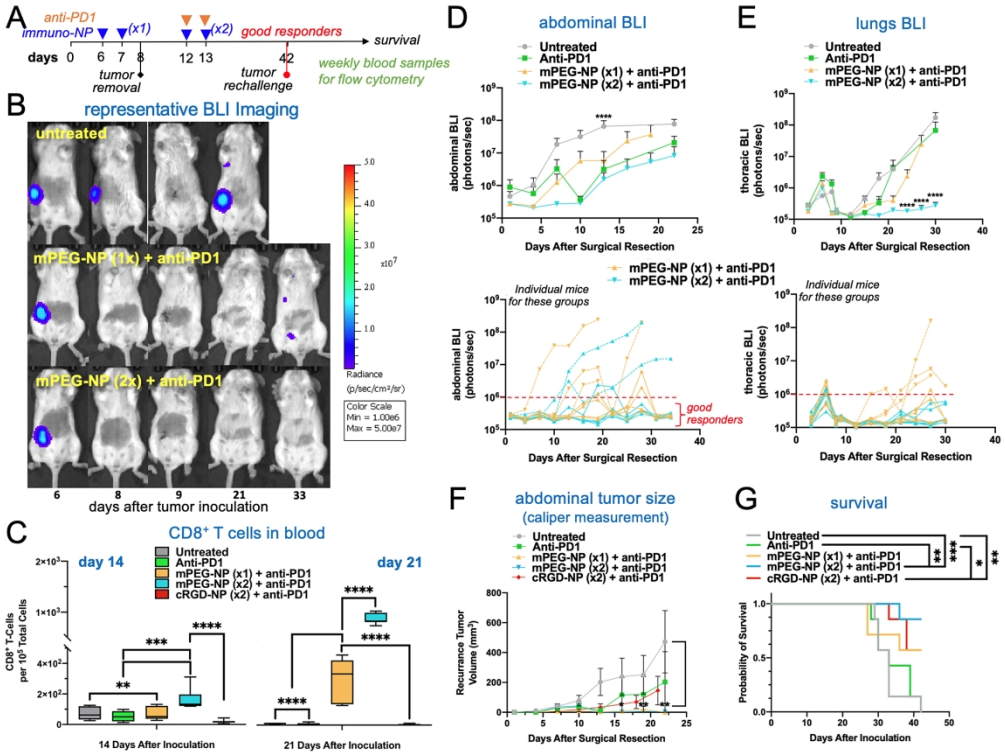

Fig. 6. Long-term efficacy of immunostimulatory NPs in combination with surgery and anti-PD1. (A) Timeline shows animal modeling, treatment schedule and related analysis. The immunostimulatory NP treatment included the untargeted NP or the integrin-targeting NP. The immunostimulatory NPs were administered on day 6 and 7 at a dose of 10 μg of cdGMP per mouse, followed by surgical resection on day 8. Some groups received a second immunostimulatory NPs (10 μg of cdGMP per mouse) on day 12 and 13 coupled with a subcutaneous administration of anti-PD1 (250 μg). (B) Representative BLI images show the progression of disease for some conditions. (C) The CD8+ T-cells in the blood was measured on day 14 and 21 using flow cytometry. (D) Caliper measurement of tumor recurrence was performed in the abdominal area. (E) Kaplan-Meier survival analysis. Quantification of BLI signal is shown for the (F) abdominal and (G) thoracic regions (top panels). The two groups that contained the untargeted NP treatment were further stratified into good and poor responders using the background BLI level (106 photons/second) as a threshold. N=7 mice per condition. Mean ☐ SEM are plotted with statistics by one-/two-way ANOVA with a post hoc Tukey or Sidak's test. *P<0.05; **P<0.01; ***P<0.001; ****P<0.0001.

254x191mm (300 x 300 DPI)

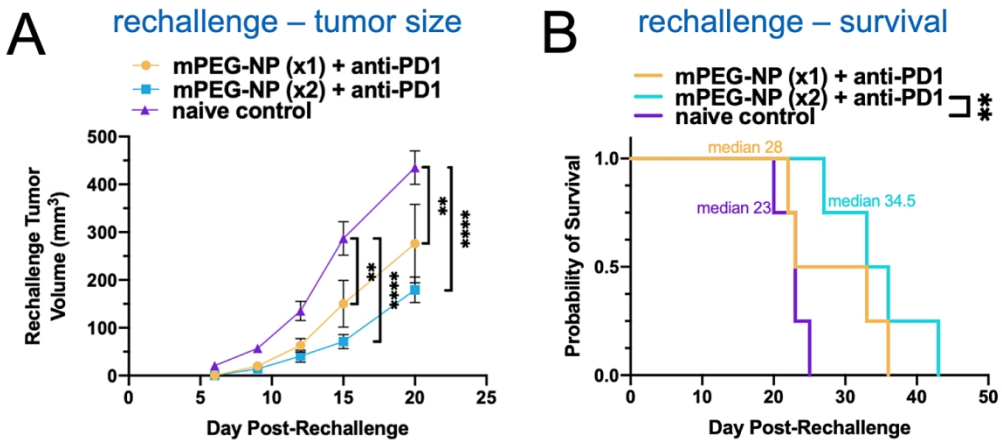

Fig. 7. Response of good responders to a tumor rechallenge. The treatment scheme of animals bearing 4T1 tumors included surgical resection of the primary tumor, anti-PD1 and untargeted immunostimulatory NP before and after surgery, indicated as mPEG-NP(x2), or only before surgery indicated as mPEG-NP(x1). The good responders from the two groups were rechallenged 42 days after the initial inoculation with 1x105 4T1 cells on their right flank. (A) Caliper measurement of the flank tumor size. (B) Kaplan-Meier survival analysis. N=4 mice per condition. Box and whisker plots (5-95 percentile) both with statistics by one-/two-way ANOVA with a post hoc Tukey or Sidak's test. **P<0.01.

127x55mm (300 x 300 DPI)